Dilution of boundary layer cloud condensation nucleus concentrations by free tropospheric entrainment during marine cold air outbreaks

Florian Tornow[1], Andrew S. Ackerman[2], Ann Fridlind[3], Brian Cairns[4], Ewan Crosbie[5], Simon Kirschler[6], Richard H Moore[7], Claire E Robinson[8], Michael Shook[9], Chellappan Seethala[10], Christiane Voigt[6], Edward L Winstead[7], Luke D. Ziemba[7], Paquita Zuidema[11], and Armin Sorooshian[12]

[1]Columbia University and NASA GISS
[2]NASA Goddard Institute for Space Studies
[3]NASA-GISS
[4]NASA GISS
[5]Universities Space Research Association
[6]Deutsches Zentrum für Luft- und Raumfahrt (DLR)
[7]NASA Langley Research Center
[8]Science Systems and Applications
[9]Langley Research Center
[10]Rosenstiel School of Marine and Atmospheric Science
[11]University of Miami/RSMAS
[12]University of Arizona

November 22, 2022

Abstract

Recent aircraft measurements over the northwest Atlantic enable an investigation of how entrainment from the free troposphere (FT) impacts cloud condensation nuclei (CCN) in the marine boundary layer (MBL) during cold-air outbreaks (CAOs), motivated by the role of CCN in mediating transitions from closed to open-cell regimes. Observations compiled over eight flights indicate predominantly far lesser CCN concentrations in the FT than in the MBL. For one flight, a fetch-dependent MBL-mean CCN budget is compiled from estimates of sea-surface fluxes, entrainment of FT air, and hydrometeor collision-coalescence, based on in-situ and remote-sensing measurements. Results indicate a dominant role of FT entrainment in reducing MBL CCN concentrations, consistent with satellite-observed trends in droplet number concentration upwind of CAO cloud-regime transitions over the northwest Atlantic. Relatively scant CCN may widely be associated with FT dry intrusions, and should accelerate cloud regime transitions where underlying MBL air is CCN-rich, thereby reducing regional albedo.

Dilution of boundary layer cloud condensation nucleus concentrations by free tropospheric entrainment during marine cold air outbreaks

F. Tornow[1,2], A. S. Ackerman[2], A. M. Fridlind[2], B. Cairns[2], E. C. Crosbie[3,4], S. Kirschler[5,6], R. H. Moore[3], C. E. Robinson[3,4], C. Seethala[7], M. A. Shook[3], C. Voigt[5,6], E. L. Winstead[3,4], L. D. Ziemba[3], P. Zuidema[7], A. Sorooshian[8,9]

[1]Earth Institute, Columbia University, NY, 10025, NY
[2]NASA Goddard Institute for Space Studies, NY, 10025, NY
[3]NASA Langley Research Center, Hampton, VA 23681, USA
[4]Science, Systems, and Applications, Inc., Hampton, VA 23681, USA
[5]Deutsches Zentrum für Luft- und Raumfahrt (DLR), Oberpfaffenhofen, Germany
[6]Johannes Gutenberg-Universität, Mainz, Germany
[7]Rosenstiel School of Marine and Atmosphere Science, University of Miami, FL, 33149, USA
[8]Department of Chemical and Environmental Engineering, University of Arizona, Tucson, Arizona, 85721, USA
[9]Department of Hydrology and Atmospheric Sciences, University of Arizona, Tucson, Arizona, 85721, USA

Key Points:

- Recent aircraft measurements enable an analysis of cloud condensation nuclei (CCN) during marine cold air outbreaks.
- CCN concentrations are usually less in the free troposphere than in the marine boundary layer over the northwest Atlantic.
- A boundary layer CCN budget indicates a leading role of entrainment dilution upwind of cloud regime transition.

Corresponding author: Florian Tornow, `florian.tornow@nasa.gov`

Abstract

Recent aircraft measurements over the northwest Atlantic enable an investigation of how entrainment from the free troposphere (FT) impacts cloud condensation nuclei (CCN) in the marine boundary layer (MBL) during cold-air outbreaks (CAOs), motivated by the role of CCN in mediating transitions from closed to open-cell regimes. Observations compiled over eight flights indicate predominantly far lesser CCN concentrations in the FT than in the MBL. For one flight, a fetch-dependent MBL-mean CCN budget is compiled from estimates of sea-surface fluxes, entrainment of FT air, and hydrometeor collision-coalescence, based on in-situ and remote-sensing measurements. Results indicate a dominant role of FT entrainment in reducing MBL CCN concentrations, consistent with satellite-observed trends in droplet number concentration upwind of CAO cloud-regime transitions over the northwest Atlantic. Relatively scant CCN may widely be associated with FT dry intrusions, and should accelerate cloud regime transitions where underlying MBL air is CCN-rich, thereby reducing regional albedo.

Plain Language Summary

Cloud droplets form on a subset of atmospheric particles, referred to as cloud condensation nuclei (CCN). The number concentration of CCN affects the brightness and horizontal extent of clouds. We use aircraft measurements from several flights where cold continental air flowing over the northwest Atlantic generates swiftly evolving clouds in the near-surface turbulent air, referred to as the marine boundary layer (MBL). We show that CCN concentrations in the immediately overlying air, the free troposphere (FT), are usually far less than in the MBL. Through additional analysis of one flight, we show that mixing of FT air is the primary factor reducing CCN concentrations in the MBL prior to rain formation.

1 Introduction

Extratropical marine boundary layer (MBL) clouds typically occupy the postfrontal sector of synoptic systems when passing over the ocean surface (e.g., Field & Wood, 2007; Rémillard & Tselioudis, 2015). Their presence substantially enhances regional albedo, and such clouds are challenging to faithfully represent in numerical models, whether for forecasting weather or projecting climate change (e.g., Bodas-Salcedo et al., 2016; Forbes & Ahlgrimm, 2014; Tselioudis et al., 2021). Common during winter and its shoulder seasons, cold air outbreaks (CAOs) pose a particular challenge (e.g., Abel et al., 2017; Field et al., 2017) as they form highly reflective, nearly overcast cloud decks, typically organized in roll-like structures that contain both water and ice, which generally break up into less reflective, open-cellular cloud fields farther downwind (e.g., Brümmer, 1999; Pithan et al., 2019).

MBL clouds are sensitive to the number concentration of aerosol available as cloud condensation nuclei (CCN). Greater CCN concentrations can enhance cloud albedo when (1) distributing the same cloud condensate over more numerous, smaller droplets (Twomey, 1974), (2) suppressing precipitation formation, leading to greater areal cloud cover (Albrecht, 1989) and thicker clouds (Pincus & Baker, 1994), and (3) affecting cloud mesoscale structure (e.g., H. Wang & Feingold, 2009). On the other hand, smaller droplets fall more slowly in updrafts and can boost entrainment of overlying dry air, reducing cloud thickness and counteracting albedo-enhancing effects (Ackerman et al., 2004; Bretherton et al., 2007). The collisions between hydrometeors that drive precipitation formation in warm clouds also reduce CCN number concentrations and can drive a positive feedback loop in which fewer CCN promote further precipitation formation in warm stratocumulus (Yamaguchi et al., 2017). Such a feedback loop is also implicated in mixed-phase CAO observations (e.g., Abel et al., 2017) and simulations (Tornow et al., 2021), and is hypothesized to explain horizontal gradients in cloud droplet number concentrations off the mid-Atlantic coast of the US (Dadashazar et al., 2021).

Unique to CAOs are extreme surface heat fluxes that typically drive rapid MBL deepening despite strong large-scale subsidence (Papritz et al., 2015; Papritz & Spengler, 2017), thereby copiously entraining free tropospheric (FT) air. Entrained FT air in turn can strongly affect MBL air, where each has been variously influenced by a wide variety of sinks and sources, including new particle formation (e.g., I. L. McCoy et al., 2021; Zheng et al., 2021) and long-range transport of direct emissions, such as biomass burning (e.g., Zheng et al., 2020).

In previous work, simulated MBL clouds in a northwest Atlantic CAO case study were found sensitive to idealized FT–MBL differences in CCN concentration (Tornow et al., 2021). The present study seeks to establish observationally the degree to which the FT serves as a CCN sink or source to the evolving cloudy MBL in CAOs in that region. This wider analysis is enabled by recent in-situ and remote-sensing observations collected on multiple research flights during the Aerosol Cloud Meteorology Interactions over the Western Atlantic Experiment (ACTIVATE; Sorooshian et al., 2019).

2 Material and Methods

We analyze all CAO research flights conducted during ACTIVATE in 2020 (Table S1). For assessment of the CCN budget, we use the second research flight on 1 March 2020 (RF14), which reached farthest downwind into the offshore cloud deck, nearly reaching the transition from overcast to broken states. For each of the eight CAO research flights in 2020, we use in-situ and remote-sensing measurements (Table S2), collected via Falcon and King Air aircraft, respectively. We collocate all in-situ data by their time stamp and associated remote-sensing products nearest in geolocation to the Falcon aircraft at a given time. Figure 1 provides a composite overview of collocated data from RF14.

The following subsections describe the CCN observations (Section 2.1), processing of data from multiple research flights (Section 2.2), and the MBL CCN budget analysis for RF14 (Section 2.3).

2.1 In-situ aerosol measurements

A Droplet Measurement Technologies (DMT) CCN counter (Roberts & Nenes, 2005; Lance et al., 2006) was operated in one of two modes:

(1) constant supersaturation (SS; usually set to 0.43%) or
(2) SS scanning (typically covering 0.2–0.7%; Moore & Nenes, 2009)

To compare data from all eight research flights (Section 3), we interpolate CCN from mode (2) operations to SS = 0.43% per leg using polynomial regression (described further below). We also use condensation nuclei (CN) counts of particles with diameters greater equal 10 nm via the TSI Condensation Particle Counters 3772 instrument.

2.2 Processing of ACTIVATE measurements

2.2.1 Classification of in-situ legs

Samples acquired at 1 Hz frequency are separated into flight legs, where each leg is defined as a consecutive period of CCN measurements uninterrupted by missing values (usually spanning ∼50 s periods). This separation triples the number of legs compared to using horizontal segments (cf. Sorooshian et al., 2019) and requires a refined leg type classification:

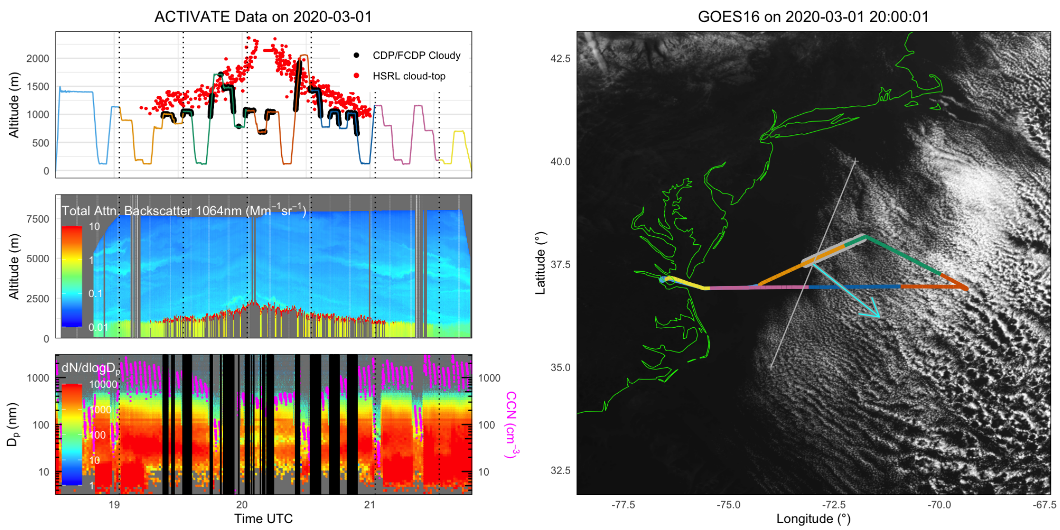

Figure 1. ACTIVATE Falcon flight track during RF14 (top left and right), King-Air remote-sensing measurements (top and middle left), Falcon in-situ measurements of aerosol PSD and CCN concentrations (bottom left), and GOES-16 image (right) with approximate wind direction inferred from roll orientation (cyan line), cloud edge (white line), and RSP measurement extent (thick gray below track).

(1) Using liquid water contents (LWCs) measured by the Fast Cloud Droplet Probe (FCDP; for particle diameters 3-50 um) and the Two-Dimensional Stereo (2DS) probe (Lawson et al., 2006, particle diameters 51-1465 um), we define cloudy samples as those with $LWC_{FCDP} + LWC_{2DS} \geq 0.05$ g m^{-3} and classify legs with at least 5 such samples as "cloudy".

(2) To classify the remaining clear legs by their relative altitude to nearby clouds, we collect the cloudy samples near each leg (within 15 min of mean leg time or within 45 min if 15 min provides fewer than 5 cloudy samples) and define the local cloud-base and cloud-top heights (CBH, CTH) from maximum and minimum altitudes, respectively, of the nearest cloudy samples (the closest 15% in time from mean leg time among samples collected) to crudely account for the spatial heterogeneity of clouds (e.g., the swiftly evolving CTH seen in Figure 1).

(3) Finally, we label each cloud-free leg by comparing its maximum and minimum altitudes (H_{max}, H_{min}) to CTH and CBH +/- a 50 m buffer to better separate FT from MBL legs and to avoid the entrainment interfacial layer (e.g., Dadashazar et al., 2018):

"clear, below-cloud":	H_{max} < (CBH - 50 m)
"clear, above-cloud":	H_{min} > (CTH + 50 m) or if
	H_{min} > (CBH - 50 m) and H_{max} > (CTH + 50 m)
	relevant for legs during ascents and descents
"clear, cloud-level":	all remaining samples above or at 500 m
"clear, near-surface":	all remaining samples below 500 m

Figure S1 shows the resulting classification for RF14, with 90 legs identified.

2.2.2 Projection into quasi-Lagrangian framework

In an ideal scenario for our analysis, all measurements would be available in a moving Lagrangian column of MBL air as it moves downwind. Lacking such a scenario, we

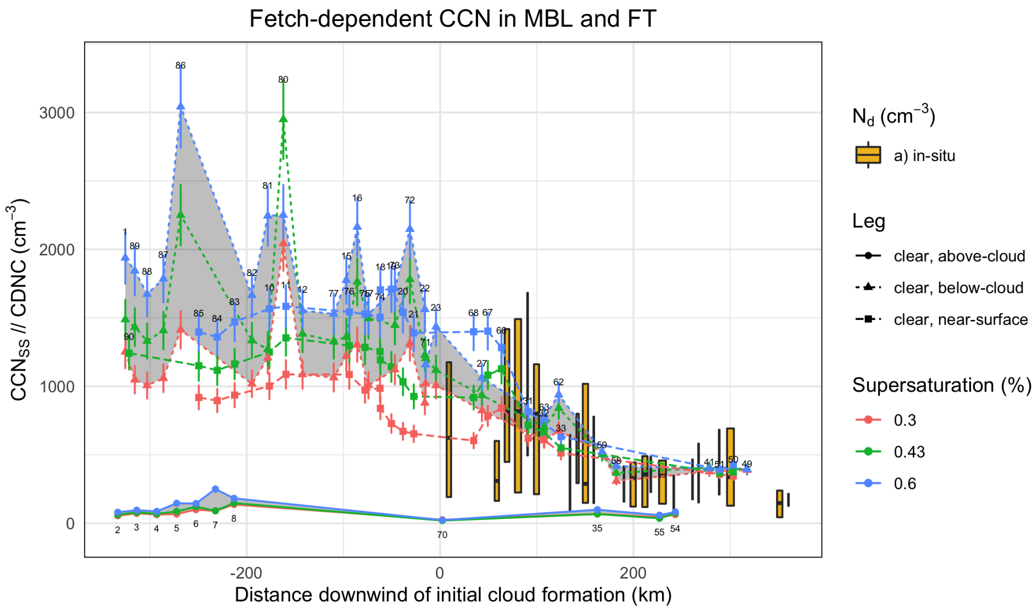

Figure 2. CCN at selected supersaturations (by color) versus ΔL derived from cloud-free samples on RF14. Leg types distinguished per legend. Gray shading spans FT class "clear, above-cloud" and MBL class "clear, below-cloud". Orange bars span middle half of in-cloud N$_d$ from FCDP, with median indicated.

roughly emulate a Lagrangian framework by projecting all measurements onto a wind field and using horizontal distance from the upwind cloud edge, ΔL, as a transformed coordinate system.

From geostationary imagery we approximate a field-wide MBL wind direction from the roll orientation, assuming zero angular offset, and draw a great circle to mark the initial cloud edge (Figure 1). We then use each leg's geolocation and the wind direction to determine the intercept point on the cloud edge up- or downwind of the leg coordinates and measure the geodetic distance between leg coordinates and this intercept point.

Figure 2 illustrates the resulting range $\Delta L \in [\pm 300$ km$]$ for RF14 corresponding to the Figure 1 scene. We note that MBL wind direction and roll orientation can be offset by up to ±20-30° (Etling & Brown, 1993; Atkinson & Wu Zhang, 1996), corresponding to a range error of about ±10 km per 100 km.

2.3 MBL CCN budget

2.3.1 Entrainment

To estimate the entrainment rate (w_e) of FT air at the top of the MBL we use CO trace gas measurements (Figure S2) and rely on a simple mixed-layer approach (e.g., Lilly, 1968; Fridlind et al., 2012) to characterize the evolution of the MBL-mean mixing ratio of species X (here applied to CO to estimate the entrainment rate, and later used for the budget of CCN$_{\mathrm{SS}=0.43\%}$). Note that we apply this approach to a horizontally translating quasi-Lagrangian domain and use MBL-averaged quantities (denoted with overbar), invoking the Lagrangian derivative:

$$\frac{d\bar{X}}{dt} = S_{\mathrm{int}} + S_{\mathrm{surf}} + S_{\mathrm{entr}} \tag{1}$$

with net sources from internal processes, surface fluxes, and FT entrainment at the MBL top (inversion base height z_i), where

$$S_{\text{entr}} = \frac{\Delta\bar{X}}{z_i} w_e \tag{2}$$

given the jump at the top of the MBL $\Delta\bar{X} = X_{\text{FT}} - \bar{X}$ and entrainment rate $w_e = \frac{dz_i}{dt} - w_{\text{LS}}$, with large-scale vertical wind w_{LS}. Internal process and surface sources are assumed zero for CO.

After combining Equations 1 and 2, we solve for w_e using the horizontal gradient in distance downwind s to evaluate the Lagrangian derivative:

$$\frac{d\bar{X}}{dt} = \frac{d\bar{X}}{ds}\frac{ds}{dt} = \frac{\bar{X}(\Delta L + 50\text{km}) - \bar{X}(\Delta L - 50\text{km})}{250\text{km}} u \tag{3}$$

with horizontal wind speed u taken at 500 m from an ERA5 profile on 1 March 2020 20:00 UTC, at 36.90°N, 69.35°W.

In these equations $\bar{X}$, X_{FT}, and z_i are computed from separate 4th-order polynomial fits versus ΔL. For fitting $\bar{X}$, we use "clear, near-surface" and "clear, below-cloud", whereas for X_{FT} we use "clear, above-cloud". For CO measurements as X_{FT} we linearly fit in-situ data (Figure S2) and for z_i we linearly fit HSRL-2 CTH (Figure S3).

Once w_e is estimated, we compute S_{entr} from Equation 2 using fits to the CCN data (Figure 2).

2.3.2 Hydrometeor collisions

We use in-situ FCDP and 2DS measurements to estimate collision-coalescence rates. We first parse the data into 5-s intervals (∼500 m horizontal distances). Per interval, we bin-wise average droplet size distributions from both instruments. We then compute collision-coalescence loss rates by integrating the simplified stochastic collection equation (cf. Wood, 2006):

$$\dot{N}_{\text{coll}} = -\frac{1}{2}\int_0^\infty \int_0^\infty n(x)K(x',x)n(x')dxdx' \tag{4}$$

in which $K(x,x')$ is the collection kernel from Hall (1980) across radius bins x and x' (assuming a coalescence efficiency of unity for simplicity):

$$K(x,x') = \pi[r(x)+r(x')]^2 E_{\text{coll}}|v(x)-v(x')| \tag{5}$$

where $n(x)$ is the measured hydrometeor number concentration, $r(x)$ the volume-mean radius for each bin, and droplet fall speed v is computed following Böhm (1992). Figure S4 shows two examples, demonstrating the impact of larger hydrometeors, as well as the estimated contribution to $\dot{N}_{\text{coll}}$ from riming computed by summing over bins with frozen hydrometeors using the same kernel.

To obtain MBL-effective collision-coalescence rates some assumptions must be made about the vertical structure of clouds within the MBL. We guide these assumptions using HSRL-2-based CTH and RSP-retrieved liquid water path (LWP) values projected onto the semi-Lagrangian framework (Section 2.2) to derive synthetic cloud profiles with stochastically drawn in-situ intervals that satisfy some proximity criteria.

We begin with RSP LWP retrievals. Discretizing the atmosphere into 50-m thick layers, we start at the layer closest to cloud top (from median of HSRL-2 CTH values within 100 s of an RSP measurement) and consider in-situ data for stochastic sampling obtained vertically within 50 m of the layer, within 100 km horizontally of the RSP observation, and within 15 min of RSP acquisition. If these criteria produce no samples, we drop spatial and temporal proximity thresholds and, if still short on samples, relax the vertical constraint. Once a layer is assigned a sample (LWC, cloud droplet number concentration N_d, and $\dot{N}_{\text{coll}}$), we proceed downward until the vertical LWC integral matches the RSP LWP, but not past cloud base (the lowest layer in which clouds were observed in-situ, ∼700 m for RF14). For large LWP values (>300 g m^{-2}), the cloud thickness is insufficient and though the reconstructed LWPs fall short, they are retained (Figure S3 inset). Figure S3 also shows profiles along ΔL and Figure S5 shows profile details. To match other budget terms we compute a 100-km running mean excluding cloud-free gaps.

Unfortunately, RSP only provides LWP values where the sun-observer geometry is favorable. For the case shown in Figure 1, these correspond to the northwest-most leg, shaded gray in Figure 4. As described further below, we use Moderate Resolution Imaging Spectroradiometer (MODIS) LWP retrievals to extend the analysis downwind.

2.3.3 Uncertainty

To estimate uncertainties, we apply Gaussian error propagation. Individual uncertainties associated with $\bar{X}$, X_{FT}, and z_i are taken from each fit's 95% confidence interval. These errors dominate when used in differentials, such as equation 3 (e.g., for $\dot{N}_{\mathrm{tot}}$ shown as dark blue bar in Figure 4). We assume 10-km uncertainty for ΔL, as already described. Assumed errors for ERA-5 variables are 10% (Seethala et al., 2021; Li et al., 2021). The error for $\dot{N}_{\mathrm{coll}}$ is estimated as the standard deviation across the locally available population, chosen because substantial sample variability (Figure S5) likely exceeds conventional error propagation.

3 Results

3.1 FT-MBL CCN gap

Figure 2 illustrates the processed CCN measurements for RF14, demonstrating the analysis approach applied to all flights. The differences between "clear, near-surface" and "clear, below-cloud" samples are smaller than the variability within each group, consistent with relatively well-mixed conditions within a turbulent MBL. Upwind of the cloud edge, entrainment of FT air can only reduce the MBL CCN, since the FT concentrations (at SS = 0.3-0.6%) are relatively stable at 50-200 cm^{-3}, much less than MBL concentrations of 1000-3000 cm^{-3}. Furthermore, the CCN gap between FT and MBL progressively narrows downwind of the cloud edge ($\Delta L > 0$ km) from decreasing MBL concentrations, consistent with dilution via strong FT entrainment (quantified below). At all downwind distances sampled during this flight, FT concentrations are well exceeded by those in the MBL.

Another prominent feature in Figure 2 is the CCN spectral width decreasing downwind of cloud formation: upwind ($\Delta L \approx$ -300 km) nearly double the particles are available for activation as SS increases from 0.3 to 0.6%, whereas downwind ($\Delta L \approx 200$ km) only ∼20% more particles are available when doubling SS, a trend likely resulting from collisions between hydrometeors affecting aerosol PSD, specifically over diameters 50–80 nm (Figure S6), and composition (Figure S7).

To assess whether the FT commonly dilutes MBL CCN in northwest Atlantic CAOs, in Figure 3a we plot MBL versus FT $\mathrm{CCN}_{\mathrm{SS}=0.43\%}$ (hereafter just "CCN") concentrations matched by ΔL. Overall, FT concentrations are predominantly exceeded by those in the MBL with rare exceptions. Some instances (e.g., "RF17 20200308-L1") may be associated with variability of upwind MBL CCN (Figure S8), discussed further in Section 4. Because supersaturations in CAO convection can be expected to exceed 0.43%, we also evaluate how particles activating at greater supersaturations affect the FT–MBL differences. We repeat our analysis using the measurement of condensation nuclei (CN) larger than 10 nm (Figure 3b), which include sizes far smaller than are likely activated in MBL clouds, and find qualitatively similar gaps.

Figure 3a also shows that the FT–MBL CCN gap generally narrows downwind of cloud formation because of decreasing MBL concentrations (open symbols tend to lie to the left of closed symbols), consistent with RF14 (Figure 2). Meanwhile, FT concentra-

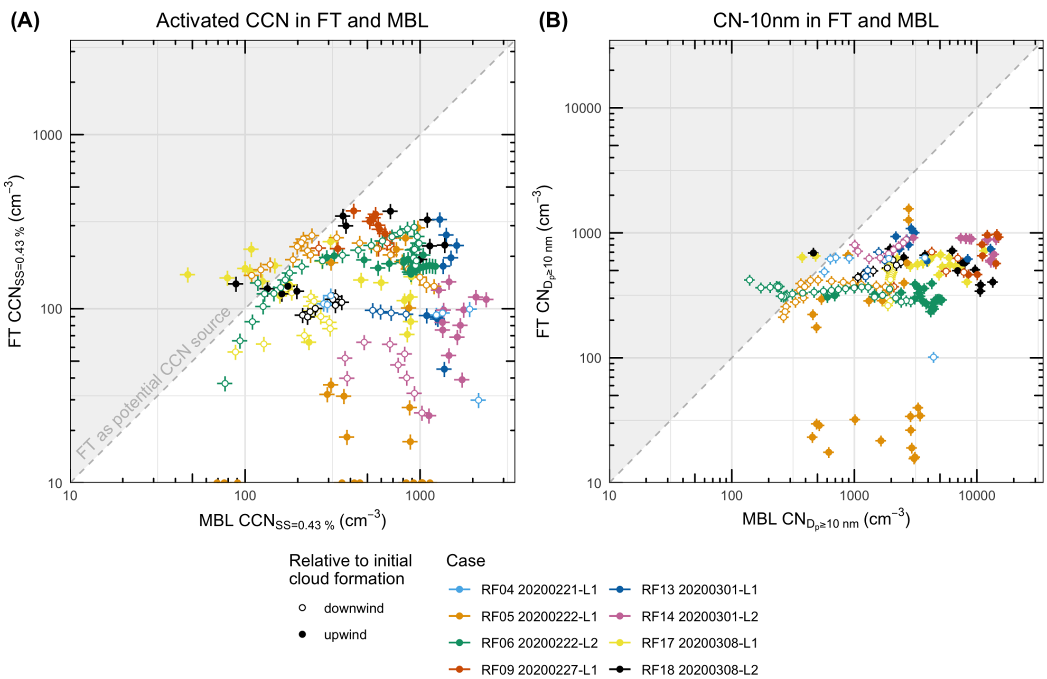

Figure 3. FT versus MBL concentration of CCN at 0.43% supersaturation (left) and of CN greater than 10 nm diameter (right) colored by research flight (per legend) and interpolated at 25-km intervals across available ΔL.

tions generally lack systematic trends with downwind distance and are characterized by a much smaller absolute dynamic range (cf. Figure 2).

3.2 Processes affecting FT–MBL gap

For RF14, we further estimate the relative contribution of FT entrainment to MBL CCN evolution. As described in Section 2, FT entrainment is approximated using CO measurements in the MBL and FT (Figure S2), yielding a rate of up to 12 cm s^{-1} for $0 < \Delta L < 100$ km (Figure S2 inset). This entrainment rate is applied to the CCN MBL–FT difference to estimate a CCN entrainment source. We also estimate a MBL-mean collision-coalescence CCN loss rate as described in Section 2 and a sea-salt surface source following Wood et al. (2017), as originally formulated by Clarke et al. (2006): $\dot{N}_{\text{surf}} = \frac{F u_s^{3.41}}{z_i}$, where $F = 132$ m^{-3} (m s^{-1})$^{-2.41}$ and near-surface wind speed u_s is taken from the ERA5 profile. This budget framework is first applied to available RSP retrievals, which for this flight are at $0 < \Delta L < 100$ km, well upwind of the cloud transition (Figure 1).

Results in Figure 4 indicate that the observed evolution in MBL CCN concentration ($\sim$ -240 cm^{-3} h^{-1}) is primarily explained by FT entrainment ($\sim$ -180 cm^{-3} h^{-1}), while hydrometeor collisions are less important ($\sim$ -25 cm^{-3} h^{-1}) and surface production is quite modest ($\sim$5 cm^{-3} h^{-1}). These relative contributions to the CCN budget are consistent with the aforementioned northwest Atlantic CAO simulations that used idealized aerosol in the absence of in situ measurements (cf. Figure 6 of Tornow et al., 2021). MODIS LWPs (acquired at 1730 UTC, 1 h before the flight) allow the budget to be extended downwind (dashed lines in Figure 4) and reveal a growing role for hydrometeor collisions approaching the cloud transition, from larger drops as well as frozen hydrometeors (riming).

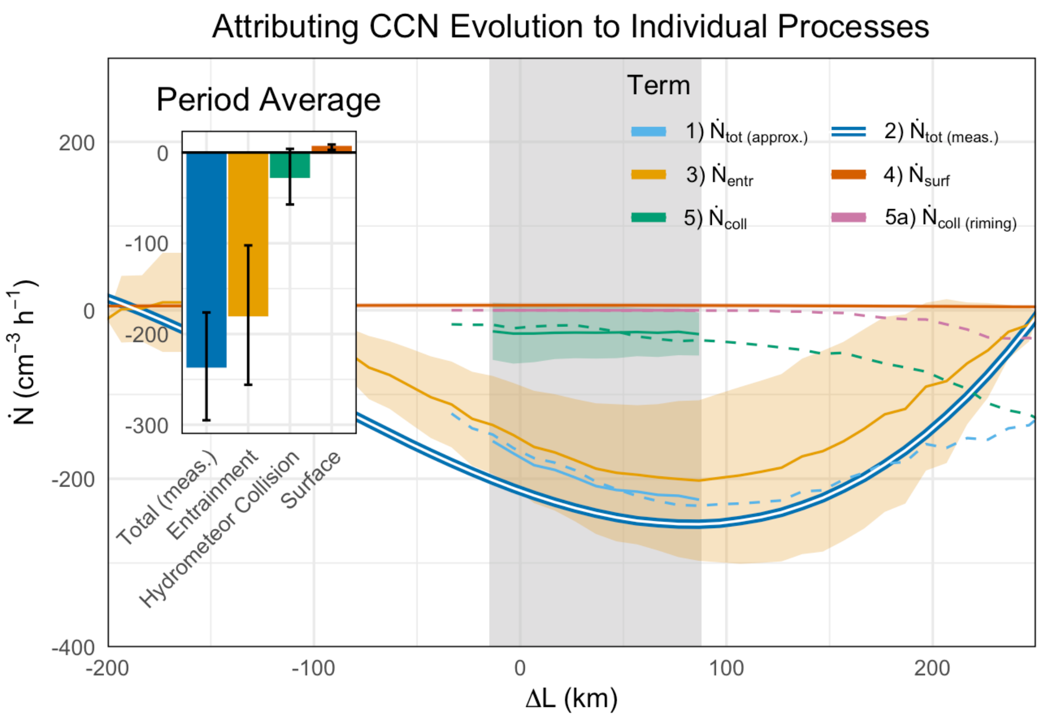

Figure 4. Quasi-Lagrangian MBL CCN budget terms versus ΔL for RF14: FT entrainment (orange), hydrometeor collisions (green) and contribution of riming (pink), surface source (red), their sum (light blue), and measured change of CCN_{SS}=0.43% (dark blue with white stripe). Rates using MODIS LWP retrievals (dashed lines) extend those from RSP (shaded area). Inset: mean values over shaded area with uncertainties (+/- one standard error).

4 Discussion

FT entrainment appears to be a plausible leading explanation for satellite-observed N_d gradients close to the US East Coast during winter (Painemal et al., 2021). Such N_d gradients are particularly strong during CAOs (Dadashazar et al., 2021), coincident with rapidly rising cloud tops despite strong large-scale subsidence (together implying great entrainment rates), and upwind of intense precipitation, where collisional loss rates are greater. Dadashazar et al. (2021) furthermore suggest a similar FT–MBL CCN difference from aerosol extinction retrievals. Our findings are also consistent with CAO simulations (Tornow et al., 2021), which yield comparable entrainment rates (Figure S2 inset) and relative roles of FT entrainment and hydrometeor collisional loss upwind of intense precipitation.

An obvious question arises: where did such relatively clean FT air originate? Back-trajectories arriving at 2 and 3 km for RF14 (Figure S9) indicate a northwest origin, respectively starting seven days earlier near Alaska and the north Pacific and reaching $\sim$6 km before subsiding. Mass spectrometry data (Figure S7) indicate an FT aerosol composed mainly of sulfate whereas MBL aerosol varies more in composition with either sulfate (downwind of cloud edge) or organics (upwind) as the dominant non-refractory component; nitrate and ammonium account for higher mass fractions in the MBL than in the FT.

We acknowledge that assuming spatiotemporal homogeneity perpendicular to the mean wind is required for our quasi-Lagrangian analysis, whereas MBL and FT properties vary upwind and across the wind. Even when a flight track aligns with MBL flow, the aircraft (speed $\sim$100 m s^{-1}) is much faster than MBL horizontal winds ($\sim$25 m s^{-1}). An example of spatial heterogeneity is evident on 8 March 2020 (Figure S8), where flight tracks are nearly perpendicular to the mean MBL wind. Samples farther offshore traveled longer periods over the ocean prior to cloud formation, and our analysis of both flights on that date indicate the FT acting briefly as a CCN source (Figure 3), which may be attributable to spatiotemporal variability neglected in our approach. Nonetheless, we expect that the quasi-Lagrangian transformation is sufficient to reveal an overall pattern of FT dilution of MBL CCN, per Figures 2 and 3.

The MBL CCN budget analysis is subject to some additional potential weaknesses. First, we use CCN at a fixed SS = 0.43%, whereas collisional loss applies to aerosol particles activated over a range of supersaturations. Second, the ERA5 reanalysis often overestimates zonal winds in the region but values are expected to be within 10% (Belmonte Rivas & Stoffelen, 2019; Seethala et al., 2021). Third, we neglect chemical sources of CCN at any given SS, such as new particle formation (although MBL total aerosol surface areas are unfavorable) and aqueous-phase processes that allow dissolved aerosol particles to activate at lower SS in subsequent cloud cycles (e.g., Y. Wang et al., 2021). Fourth, a chain of assumptions is required to construct MBL cloud profiles for collision-coalescence calculations. The sizable error bars in Figure 4 are intended to include these uncertainties.

Finally, we note that previous CAO observations (Abel et al., 2017) and simulations (Tornow et al., 2021) indicate even more rapid CCN loss during formation of intense precipitation. Based on inspection of cloud-regime transitions in satellite images compared with 2020 ACTIVATE CAO flight tracks, intense precipitation systematically occurs farther downwind than the observations analyzed here and could lead to reversal of the sign of the MBL–FT difference. CCN dilution from FT entrainment should accelerate this precipitation formation and subsequent transition towards open-cellular clouds.

The MBL aerosol entrainment documented here over the northwest Atlantic should widely occur in CAOs subject to FT dry intrusions (e.g., Jaeglé et al., 2017; Raveh-Rubin, 2017), which bring descending air from higher altitudes with relatively low CCN concentrations. CCN dilution is expected where the MBL is polluted, downwind of continental CCN source regions. Earth system model results may be sensitive to precipitation formation in such CAOs (D. T. McCoy et al., 2020), indicating a need to capture such aerosol dynamics in order to faithfully simulate cloud regime transitions.

5 Conclusions

A quasi-Lagrangian analysis of recent measurements collected during the ACTIVATE field campaign is developed that supports the following conclusions:

- Cloud condensation nucleus (CCN) concentrations in the marine boundary layer (MBL) at supersaturations of 0.3 to 0.6%, as well as condensation nuclei larger than 10 nm, are predominantly far greater than in the free troposphere (FT) during cold-air outbreaks (CAOs) over the northwest Atlantic.
- Based on the research flight that reached farthest downwind, a budget analysis of CCN concentration in the MBL computed from available in-situ and remote-sensing measurements identifies MBL dilution from rapid entrainment of FT air as the primary sink of CCN upwind of cloud-regime transitions.
- CCN dilution from FT entrainment should accelerate precipitation formation and cloud closed-to-open cell transitions, reducing regional albedo in CAOs fed by similar FT air masses that are often associated with dry intrusions.

Open Research

All data is available at `https://www-air.larc.nasa.gov/cgi-bin/ArcView/activate.2019`. The R code written to evaluate data is available upon request.

Acknowledgments

This work was supported by ACTIVATE, a NASA Earth Venture Suborbital-3 (EVS-3) investigation funded by NASA's Earth Science Division and managed through the Earth System Science Pathfinder Program Office Division (grant no. 80NSSC19K044). We thank the ACTIVATE team for helpful discussion and for support with measurements and quality control. Support by the German Science Foundation DFG within the SPP HALO 1294 under grants VO1504/5-1, VO1504/7-1, and of the CRC TRR 301/1 TP Change is acknowledged.

References

Abel, S. J., Boutle, I. A., Waite, K., Fox, S., Brown, P. R. A., Cotton, R., ... Bower, K. N. (2017). The role of precipitation in controlling the transition from stratocumulus to cumulus clouds in a northern hemisphere cold-air outbreak. *Journal of the Atmospheric Sciences*, *74*(7), 2293 - 2314. Retrieved from `https://journals.ametsoc.org/view/journals/atsc/74/7/jas-d-16-0362.1.xml` doi: 10.1175/JAS-D-16-0362.1

Ackerman, A. S., Kirkpatrick, M., & Stevens, D. (2004). The impact of humidity above stratiform clouds on indirect aerosol climate forcing. *Nature*, *432*, 1014–1017. Retrieved from `https://www.nature.com/articles/nature03174` doi: 10.1038/nature03174

Albrecht, B. A. (1989). Aerosols, cloud microphysics, and fractional cloudiness. *Science*, *245*(4923), 1227-1230. Retrieved from `https://www.science.org/doi/10.1126/science.245.4923.1227` doi: 10.1126/science.245.4923.1227

Atkinson, B. W., & Wu Zhang, J. (1996). Mesoscale shallow convection in the atmosphere. *Reviews of Geophysics*, *34*(4), 403-431. Retrieved from `https://agupubs.onlinelibrary.wiley.com/doi/abs/10.1029/96RG02623` doi: https://doi.org/10.1029/96RG02623

Belmonte Rivas, M., & Stoffelen, A. (2019). Characterizing era-interim and era5 surface wind biases using ascat. *Ocean Science*, *15*(3), 831–852. Retrieved from https://os.copernicus.org/articles/15/831/2019/ doi: 10.5194/os-15-831-2019

Bodas-Salcedo, A., Hill, P. G., Furtado, K., Williams, K. D., Field, P. R., Manners, J. C., ... Kato, S. (2016). Large contribution of supercooled liquid clouds to the solar radiation budget of the southern ocean. *Journal of Climate*, *29*(11), 4213 - 4228. Retrieved from https://journals.ametsoc.org/view/journals/clim/29/11/jcli-d-15-0564.1.xml doi: 10.1175/JCLI-D-15-0564.1

Bretherton, C. S., Blossey, P. N., & Uchida, J. (2007). Cloud droplet sedimentation, entrainment efficiency, and subtropical stratocumulus albedo. *Geophysical Research Letters*, *34*(3). Retrieved from https://agupubs.onlinelibrary.wiley.com/doi/abs/10.1029/2006GL027648 doi: https://doi.org/10.1029/2006GL027648

Brümmer, B. (1999). Roll and cell convection in wintertime arctic cold-air outbreaks. *Journal of the Atmospheric Sciences*, *56*(15), 2613 - 2636. Retrieved from https://journals.ametsoc.org/view/journals/atsc/56/15/1520-0469_1999_056_2613_racciw_2.0.co_2.xml doi: 10.1175/1520-0469(1999)056⟨2613:RACCIW⟩2.0.CO;2

Böhm, J. P. (1992). A general hydrodynamic theory for mixed-phase microphysics. part i: drag and fall speed of hydrometeors. *Atmospheric Research*, *27*(4), 253-274. Retrieved from https://www.sciencedirect.com/science/article/pii/0169809592900359 doi: https://doi.org/10.1016/0169-8095(92)90035-9

Clarke, A. D., Owens, S. R., & Zhou, J. (2006). An ultrafine sea-salt flux from breaking waves: Implications for cloud condensation nuclei in the remote marine atmosphere. *Journal of Geophysical Research: Atmospheres*, *111*(D6). Retrieved from https://agupubs.onlinelibrary.wiley.com/doi/abs/10.1029/2005JD006565 doi: 10.1029/2005JD006565

Dadashazar, H., Braun, R. A., Crosbie, E., Chuang, P. Y., Woods, R. K., Jonsson, H. H., & Sorooshian, A. (2018). Aerosol characteristics in the entrainment interface layer in relation to the marine boundary layer and free troposphere. *Atmospheric Chemistry and Physics*, *18*(3), 1495–1506. Retrieved from https://acp.copernicus.org/articles/18/1495/2018/ doi: 10.5194/acp-18-1495-2018

Dadashazar, H., Painemal, D., Alipanah, M., Brunke, M., Chellappan, S., Corral, A. F., ... Sorooshian, A. (2021). Cloud drop number concentrations over the western north atlantic ocean: seasonal cycle, aerosol interrelationships, and other influential factors. *Atmospheric Chemistry and Physics*, *21*(13), 10499–10526. Retrieved from https://acp.copernicus.org/articles/21/10499/2021/ doi: 10.5194/acp-21-10499-2021

Etling, D., & Brown, R. A. (1993). Roll vortices in the planetary boundary layer: A review. *Boundary-Layer Meteorology*, *65*(3), 215–248. Retrieved from https://link.springer.com/article/10.1007/BF00705527 doi: 10.1007/BF00705527

Field, P. R., Brozkova, R., Chen, M., Dudhia, J., Lac, C., Hara, T., ... McTaggart-Cowan, R. (2017). Exploring the convective grey zone with regional simulations of a cold air outbreak. *Quarterly Journal of the Royal Meteorological Society*, *143*(707), 2537-2555. Retrieved from https://rmets.onlinelibrary.wiley.com/doi/full/10.1002/qj.3105 doi: https://doi.org/10.1002/qj.3105

Field, P. R., & Wood, R. (2007). Precipitation and cloud structure in midlatitude cyclones. *Journal of Climate*, *20*(2), 233 - 254. Retrieved from https://journals.ametsoc.org/view/journals/clim/20/2/jcli3998.1.xml doi: 10.1175/JCLI3998.1

Forbes, R. M., & Ahlgrimm, M. (2014). On the representation of high-latitude boundary layer mixed-phase cloud in the ecmwf global model. *Monthly Weather Review*, *142*(9), 3425 - 3445. Retrieved from https://journals.ametsoc.org/view/journals/mwre/142/9/mwr-d-13-00325.1.xml doi: 10.1175/MWR-D-13-00325.1

Fridlind, A. M., Ackerman, A. S., Chaboureau, J.-P., Fan, J., Grabowski, W. W., Hill, A. A., ... Zhang, M. (2012). A comparison of twp-ice observational data with cloud-resolving model results. *Journal of Geophysical Research: Atmospheres*, *117*(D5). Retrieved from https://agupubs.onlinelibrary.wiley.com/doi/abs/10.1029/2011JD016595 doi: 10.1029/2011JD016595

Hall, W. D. (1980). A detailed microphysical model within a two-dimensional dynamic framework: Model description and preliminary results. *Journal of Atmospheric Sciences*, *37*(11), 2486 - 2507. Retrieved from https://journals.ametsoc.org/view/journals/atsc/37/11/1520-0469_1980_037_2486_admmwa_2_0_co_2.xml doi: 10.1175/1520-0469(1980)037⟨2486:ADMMWA⟩2.0.CO;2

Jaeglé, L., Wood, R., & Wargan, K. (2017). Multiyear composite view of ozone enhancements and stratosphere-to-troposphere transport in dry intrusions of northern hemisphere extratropical cyclones. *Journal of Geophysical Research: Atmospheres*, *122*(24), 13,436-13,457. Retrieved from https://agupubs.onlinelibrary.wiley.com/doi/abs/10.1002/2017JD027656 doi: https://doi.org/10.1002/2017JD027656

Lance, S., Nenes, A., Medina, J., & Smith, J. N. (2006). Mapping the operation of the dmt continuous flow ccn counter. *Aerosol Science and Technology*, *40*(4), 242-254. Retrieved from https://doi.org/10.1080/02786820500543290 doi: 10.1080/02786820500543290

Lawson, R. P., O'Connor, D., Zmarzly, P., Weaver, K., Baker, B., Mo, Q., & Jonsson, H. (2006). The 2d-s (stereo) probe: Design and preliminary tests of a new airborne, high-speed, high-resolution particle imaging probe. *Journal of Atmospheric and Oceanic Technology*, *23*(11), 1462 - 1477. Retrieved from https://journals.ametsoc.org/view/journals/atot/23/11/jtech1927_1.xml doi: 10.1175/JTECH1927.1

Li, X.-Y., Wang, H., Chen, J., Endo, S., George, G., Cairns, B., ... Zuidema, P. (2021). Large-eddy simulations of marine boundary-layer clouds associated with cold air outbreaks during the activate campaign– part 1: Case setup and sensitivities to large-scale forcings. *Journal of the Atmospheric Sciences*. Retrieved from https://journals.ametsoc.org/view/journals/atsc/aop/JAS-D-21-0123.1/JAS-D-21-0123.1.xml doi: 10.1175/JAS-D-21-0123.1

Lilly, D. K. (1968). Models of cloud-topped mixed layers under a strong inversion. *Quarterly Journal of the Royal Meteorological Society*, *94*(401), 292-309. Retrieved from https://rmets.onlinelibrary.wiley.com/doi/abs/10.1002/qj.49709440106 doi: https://doi.org/10.1002/qj.49709440106

McCoy, D. T., Field, P., Bodas-Salcedo, A., Elsaesser, G. S., & Zelinka, M. D. (2020). A regime-oriented approach to observationally constraining extratropical shortwave cloud feedbacks. *Journal of Climate*, *33*(23), 9967 - 9983. Retrieved from https://journals.ametsoc.org/view/journals/clim/33/23/jcliD190987.xml doi: 10.1175/JCLI-D-19-0987.1

McCoy, I. L., Bretherton, C. S., Wood, R., Twohy, C. H., Gettelman, A., Bardeen, C. G., & Toohey, D. W. (2021). Influences of recent particle formation on southern ocean aerosol variability and low cloud properties. *Journal of Geophysical Research: Atmospheres*, *126*(8), e2020JD033529. Retrieved from https://agupubs.onlinelibrary.wiley.com/doi/abs/10.1029/2020JD033529 doi: https://doi.org/10.1029/2020JD033529

Moore, R. H., & Nenes, A. (2009). Scanning flow ccn analysis—a method for fast measurements of ccn spectra. *Aerosol Science and Technology*, *43*(12), 1192-

1207. Retrieved from https://doi.org/10.1080/02786820903289780 doi: 10.1080/02786820903289780

Painemal, D., Corral, A. F., Sorooshian, A., Brunke, M. A., Chellappan, S., Afzali Gorooh, V., ... Zuidema, P. (2021). An overview of atmospheric features over the western north atlantic ocean and north american east coast—part 2: Circulation, boundary layer, and clouds. *Journal of Geophysical Research: Atmospheres*, *126*(6), e2020JD033423. Retrieved from https://agupubs.onlinelibrary.wiley.com/doi/abs/10.1029/2020JD033423 doi: https://doi.org/10.1029/2020JD033423

Papritz, L., Pfahl, S., Sodemann, H., & Wernli, H. (2015). A climatology of cold air outbreaks and their impact on air–sea heat fluxes in the high-latitude south pacific. *Journal of Climate*, *28*(1), 342 - 364. Retrieved from https://journals.ametsoc.org/view/journals/clim/28/1/jcli-d-14-00482.1.xml doi: 10.1175/JCLI-D-14-00482.1

Papritz, L., & Spengler, T. (2017). A lagrangian climatology of wintertime cold air outbreaks in the irminger and nordic seas and their role in shaping air–sea heat fluxes. *Journal of Climate*, *30*(8), 2717 - 2737. Retrieved from https://journals.ametsoc.org/view/journals/clim/30/8/jcli-d-16-0605.1.xml doi: 10.1175/JCLI-D-16-0605.1

Pincus, R., & Baker, M. B. (1994). Effect of precipitation on the albedo susceptibility of clouds in the marine boundary layer. *Nature*, *372*(6503), 250 - 252. Retrieved from https://www.nature.com/articles/372250a0 doi: 10.1038/372250a0

Pithan, F., Svensson, G., Caballero, R., Chechin, D., Cronin, T. W., Ekman, A. M. L., ... Wendisch, M. (2019). Role of air-mass transformations in exchange between the arctic and mid-latitudes. *Nature Geoscience*, *11*, 805–812. Retrieved from https://www.nature.com/articles/s41561-018-0234-1 doi: 10.1038/s41561-018-0234-1

Raveh-Rubin, S. (2017). Dry intrusions: Lagrangian climatology and dynamical impact on the planetary boundary layer. *Journal of Climate*, *30*(17), 6661 - 6682. Retrieved from https://journals.ametsoc.org/view/journals/clim/30/17/jcli-d-16-0782.1.xml doi: 10.1175/JCLI-D-16-0782.1

Roberts, G. C., & Nenes, A. (2005). A continuous-flow streamwise thermal-gradient ccn chamber for atmospheric measurements. *Aerosol Science and Technology*, *39*(3), 206-221. Retrieved from https://doi.org/10.1080/027868290913988 doi: 10.1080/027868290913988

Rémillard, J., & Tselioudis, G. (2015). Cloud regime variability over the azores and its application to climate model evaluation. *Journal of Climate*, *28*(24), 9707 - 9720. Retrieved from https://journals.ametsoc.org/view/journals/clim/28/24/jcli-d-15-0066.1.xml doi: 10.1175/JCLI-D-15-0066.1

Seethala, C., Zuidema, P., Edson, J., Brunke, M., Chen, G., Li, X.-Y., ... Ziemba, L. (2021). On assessing era5 and merra2 representations of cold-air outbreaks across the gulf stream. *Geophysical Research Letters*, *48*(19), e2021GL094364. Retrieved from https://agupubs.onlinelibrary.wiley.com/doi/abs/10.1029/2021GL094364 doi: https://doi.org/10.1029/2021GL094364

Sorooshian, A., Anderson, B., Bauer, S. E., Braun, R. A., Cairns, B., Crosbie, E., ... Zuidema, P. (2019). Aerosol–cloud–meteorology interaction airborne field investigations: Using lessons learned from the u.s. west coast in the design of activate off the u.s. east coast. *Bulletin of the American Meteorological Society*, *100*(8), 1511 – 1528. Retrieved from https://journals.ametsoc.org/view/journals/bams/100/8/bams-d-18-0100.1.xml doi: 10.1175/BAMS-D-18-0100.1

Tornow, F., Ackerman, A. S., & Fridlind, A. M. (2021). Preconditioning of overcast-to-broken cloud transitions by riming in marine cold air outbreaks. *Atmospheric Chemistry and Physics*, *21*(15), 12049–12067. Retrieved from https://acp.copernicus.org/articles/21/12049/2021/ doi: 10.5194/acp-21-12049-2021

Tselioudis, G., Rossow, W. B., Jakob, C., Remillard, J., Tropf, D., & Zhang, Y. (2021). Evaluation of clouds, radiation, and precipitation in cmip6 models using global weather states derived from isccp-h cloud property data. *Journal of Climate*, *34*(17), 7311 - 7324. Retrieved from https://journals.ametsoc.org/view/journals/clim/aop/JCLI-D-21-0076.1/JCLI-D-21-0076.1.xml doi: 10.1175/JCLI-D-21-0076.1

Twomey, S. (1974). Pollution and the planetary albedo. *Atmospheric Environment (1967)*, *8*(12), 1251-1256. Retrieved from https://www.sciencedirect.com/science/article/pii/0004698174900043 doi: https://doi.org/10.1016/0004-6981(74)90004-3

Wang, H., & Feingold, G. (2009). Modeling mesoscale cellular structures and drizzle in marine stratocumulus. part i: Impact of drizzle on the formation and evolution of open cells. *Journal of the Atmospheric Sciences*, *66*(11), 3237 - 3256. Retrieved from https://journals.ametsoc.org/view/journals/atsc/66/11/2009jas3022.1.xml doi: 10.1175/2009JAS3022.1

Wang, Y., Zheng, G., Jensen, M. P., Knopf, D. A., Laskin, A., Matthews, A. A., ... Wang, J. (2021). Vertical profiles of trace gas and aerosol properties over the eastern north atlantic: variations with season and synoptic condition. *Atmospheric Chemistry and Physics*, *21*(14), 11079–11098. Retrieved from https://acp.copernicus.org/articles/21/11079/2021/ doi: 10.5194/acp-21-11079-2021

Wood, R. (2006). Rate of loss of cloud droplets by coalescence in warm clouds. *Journal of Geophysical Research: Atmospheres*, *111*(D21). Retrieved from https://agupubs.onlinelibrary.wiley.com/doi/abs/10.1029/2006JD007553 doi: https://doi.org/10.1029/2006JD007553

Wood, R., Stemmler, J. D., Rémillard, J., & Jefferson, A. (2017). Low-ccn concentration air masses over the eastern north atlantic: Seasonality, meteorology, and drivers. *Journal of Geophysical Research: Atmospheres*, *122*(2), 1203-1223. Retrieved from https://agupubs.onlinelibrary.wiley.com/doi/abs/10.1002/2016JD025557 doi: 10.1002/2016JD025557

Yamaguchi, T., Feingold, G., & Kazil, J. (2017). Stratocumulus to cumulus transition by drizzle. *Journal of Advances in Modeling Earth Systems*, *9*(6), 2333-2349. Retrieved from https://agupubs.onlinelibrary.wiley.com/doi/full/10.1002/2017MS001104 doi: 10.1002/2017MS001104

Zheng, G., Sedlacek, A. J., Aiken, A. C., Feng, Y., Watson, T. B., Raveh-Rubin, S., ... Wang, J. (2020). Long-range transported north american wildfire aerosols observed in marine boundary layer of eastern north atlantic. *Environment International*, *139*, 105680. Retrieved from https://www.sciencedirect.com/science/article/pii/S0160412019326480 doi: https://doi.org/10.1016/j.envint.2020.105680

Zheng, G., Wang, Y., Wood, R., Jensen, M. P., Kuang, C., McCoy, I. L., ... Wang, J. (2021). New particle formation in the remote marine boundary layer. *Nature Communications*, *12*(1), 527. Retrieved from https://www.nature.com/articles/s41467-020-20773-1 doi: 10.1038/s41467-020-20773-1

Supporting Information for "Dilution of boundary layer cloud condensation nucleus concentrations by free tropospheric entrainment during marine cold air outbreaks"

F. Tornow[1,2], A. S. Ackerman[2], A. M. Fridlind[2], B. Cairns[2], E. C. Crosbie[3,4], S. Kirschler[5,6], R. H. Moore[3], C. E. Robinson[3,4], C. Seethala[7], M. A. Shook[3], C. Voigt[5,6], E. L. Winstead[3,4], L. D. Ziemba[3], P. Zuidema[7], A. Sorooshian[8,9]

[1]Earth Institute, Columbia University, NY, 10025, NY

[2]NASA Goddard Institute for Space Studies, NY, 10025, NY

[3]NASA Langley Research Center, Hampton, VA 23681, USA

[4]Science, Systems, and Applications, Inc., Hampton, VA 23681, USA

[5]Deutsches Zentrum für Luft- und Raumfahrt (DLR), Oberpfaffenhofen, Germany

[6]Johannes Gutenberg-Universität, Mainz, Germany

[7]Rosenstiel School of Marine and Atmosphere Science, University of Miami, FL, 33149, USA

[8]Department of Chemical and Environmental Engineering, University of Arizona, Tucson, Arizona, 85721, USA

[9]Department of Hydrology and Atmospheric Sciences, University of Arizona, Tucson, Arizona, 85721, USA

Contents of this file

2. Tables S1 to S2

References

Burton, S. P., Hostetler, C. A., Cook, A. L., Hair, J. W., Seaman, S. T., Scola, S., ... Müller, D. (2018, Jul). Calibration of a high spectral resolution lidar using a michelson interferometer, with data examples from oracles. *Appl. Opt.*, *57*(21), 6061–6075. Retrieved from `http://www.osapublishing.org/ao/abstract.cfm?URI=ao-57-21-6061` doi: 10.1364/AO.57.006061

Cairns, B., Russell, E. E., & Travis, L. D. (1999). Research Scanning Polarimeter: calibration and ground-based measurements. In D. H. Goldstein & D. B. Chenault (Eds.), *Polarization: Measurement, analysis, and remote sensing ii* (Vol. 3754, pp. 186 – 196). SPIE. Retrieved from `https://doi.org/10.1117/12.366329` doi: 10.1117/12.366329

DeCarlo, P. F., Dunlea, E. J., Kimmel, J. R., Aiken, A. C., Sueper, D., Crounse, J., ... Jimenez, J. L. (2008). Fast airborne aerosol size and chemistry measurements above mexico city and central mexico during the milagro campaign. *Atmospheric Chemistry and Physics*, *8*(14), 4027–4048. Retrieved from `https://acp.copernicus.org/articles/8/4027/2008/` doi: 10.5194/acp-8-4027-2008

Froyd, K. D., Murphy, D. M., Brock, C. A., Campuzano-Jost, P., Dibb, J. E., Jimenez, J.-L., ... Ziemba, L. D. (2019). A new method to quantify mineral dust and other aerosol species from aircraft platforms using single-particle mass spectrometry. *Atmospheric Measurement Techniques*, *12*(11), 6209–6239. Retrieved from `https://amt.copernicus.org/articles/12/6209/2019/` doi: 10.5194/amt-12-6209-2019

Hock, T. F., & Franklin, J. L. (1999). The ncar gps dropwindsonde. *Bulletin of the American Meteorological Society*, *80*(3), 407 - 420. Retrieved from https://journals.ametsoc.org/view/journals/bams/80/3/1520-0477_1999_080_0407_tngd_2_0_co_2.xml doi: 10.1175/1520-0477(1999)080⟨0407:TNGD⟩2.0.CO;2

Kleine, J., Voigt, C., Sauer, D., Schlager, H., Scheibe, M., Jurkat-Witschas, T., … Anderson, B. E. (2018). In situ observations of ice particle losses in a young persistent contrail. *Geophysical Research Letters*, *45*(24), 13,553-13,561. Retrieved from https://agupubs.onlinelibrary.wiley.com/doi/abs/10.1029/2018GL079390 doi: https://doi.org/10.1029/2018GL079390

Knop, I., Bansmer, S. E., Hahn, V., & Voigt, C. (2021). Comparison of different droplet measurement techniques in the braunschweig icing wind tunnel. *Atmospheric Measurement Techniques*, *14*(2), 1761–1781. Retrieved from https://amt.copernicus.org/articles/14/1761/2021/ doi: 10.5194/amt-14-1761-2021

Lance, S., Nenes, A., Medina, J., & Smith, J. N. (2006). Mapping the operation of the dmt continuous flow ccn counter. *Aerosol Science and Technology*, *40*(4), 242-254. Retrieved from https://doi.org/10.1080/02786820500543290 doi: 10.1080/02786820500543290

Lawson, R. P., O'Connor, D., Zmarzly, P., Weaver, K., Baker, B., Mo, Q., & Jonsson, H. (2006). The 2d-s (stereo) probe: Design and preliminary tests of a new airborne, high-speed, high-resolution particle imaging probe. *Journal of Atmospheric and Oceanic Technology*, *23*(11), 1462 - 1477. Retrieved from https://journals.ametsoc.org/

view/journals/atot/23/11/jtech1927_1.xml doi: 10.1175/JTECH1927.1

Moore, R. H., Thornhill, K. L., Weinzierl, B., Sauer, D., D'Ascoli, E., Kim, J., … Anderson, B. E. (2017). Biofuel blending reduces particle emissions from aircraft engines at cruise conditions. *Nature*, *543*, 411-415. Retrieved from https://www.nature.com/articles/nature21420 doi: 10.1038/nature21420

Rolph, G., Stein, A., & Stunder, B. (2017). Real-time environmental applications and display system: Ready. *Environmental Modelling & Software*, *95*, 210-228. Retrieved from https://www.sciencedirect.com/science/article/pii/S1364815217302360 doi: https://doi.org/10.1016/j.envsoft.2017.06.025

Sorooshian, A., Brechtel, F. J., Ma, Y., Weber, R. J., Corless, A., Flagan, R. C., & Seinfeld, J. H. (2006). Modeling and characterization of a particle-into-liquid sampler (pils). *Aerosol Science and Technology*, *40*(6), 396-409. Retrieved from https://doi.org/10.1080/02786820600632282 doi: 10.1080/02786820600632282

Stein, A. F., Draxler, R. R., Rolph, G. D., Stunder, B. J. B., Cohen, M. D., & Ngan, F. (2015). Noaa's hysplit atmospheric transport and dispersion modeling system. *Bulletin of the American Meteorological Society*, *96*(12), 2059 - 2077. Retrieved from https://journals.ametsoc.org/view/journals/bams/96/12/bams-d-14-00110.1.xml doi: 10.1175/BAMS-D-14-00110.1

Taylor, J. W., Haslett, S. L., Bower, K., Flynn, M., Crawford, I., Dorsey, J., … Coe, H. (2019). Aerosol influences on low-level clouds in the west african monsoon. *Atmospheric Chemistry and Physics*, *19*(13), 8503–8522. Retrieved from https://acp.copernicus.org/articles/19/8503/2019/ doi: 10.5194/acp-19-8503-2019

Tornow, F., Ackerman, A. S., & Fridlind, A. M. (2021). Preconditioning of overcast-to-broken cloud transitions by riming in marine cold air outbreaks. *Atmospheric Chemistry and Physics*, *21*(15), 12049–12067. Retrieved from https://acp.copernicus.org/articles/21/12049/2021/ doi: 10.5194/acp-21-12049-2021

Table S1. 2020 ACTIVATE CAO research flights, the prevalent MBL wind direction, coordinates defining the initial cloud edge, and instrument limitations relevant to this study (see text).

Date / Leg	#	Wind Dir.	Cloud edge coordinates	Instrument Limitations
2020-02-21 / 1	RF04	20°	38.0°N 76.4°W – 39.5°N 72.0°W	Falcon only
2020-02-22 / 1	RF05	25°	34.0°N 77.4°W – 38.0°N 71.5°W	Falcon only
2020-02-22 / 2	RF06	25°	34.0°N 77.4°W – 38.0°N 71.5°W	Falcon only
2020-02-27 / 1	RF09	300°	34.0°N 76.0°W – 38.0°N 73.0°W	/
2020-03-01 / 1	RF13	315°	35.0°N 75.0°W – 40.0°N 72.0°W	/
2020-03-01 / 2	RF14	315°	35.0°N 74.0°W – 40.0°N 72.0°W	/
2020-03-08 / 1	RF17	10°	33.0°N 77.0°W – 36.5°N 72.0°W	No RSP
2020-03-08 / 2	RF18	20°	34.5°N 78.0°W – 34.5°N 70.0°W	No RSP

Table S2. Instruments, products, and estimated uncertainty used.

Instrument (in-situ)	**Used Products**	**Uncertainty**	**Reference**
DMT CCN Counter	CCN(s), for either SS=0.43% or SS $\in$ [0.2,0.7%]	ΔSS=0.04, δCCN=10%	Lance, Nenes, Medina, and Smith (2006)
TSI CPC-3772	CN-10nm	10%	/
TSI LAS	dNa/dlogD for D $\in$ [0.1,3.1 um]	20%	Froyd et al. (2019)
SMPS	dNa/dlogD for D $\in$ [0.003,0.089 um]	20%	Moore et al. (2017)
PILS	Mass conc. for D $\in$ [0.05,4.00 um]	/	Sorooshian et al. (2006)
AMS	Mass conc. for D $\in$ [0.06,0.60 um]	<50%	DeCarlo et al. (2008)
SPEC FCDP	dNd/dlogD for D $\in$ [3.0,50 um], LWP	/	Knop, Bansmer, Hahn, and Voigt (2021)
SPEC 2DS	dNd/dlogD for D $\in$ [30,1460 um], LWP, IWC	/	Lawson et al. (2006) Kleine et al. (2018) Taylor et al. (2019)
PICARRO G2401-m	CO gas concentration	2%	/
Instrument (remote)			
HSRL-2	Cloud-top height		Burton et al. (2018)
RSP	Cloud optical thickness, Droplet effective radius	15%	Cairns, Russell, and Travis (1999)
Dropsonde	Temperature, Pressure	0.2 K and 0.05 hPa	Hock and Franklin (1999)

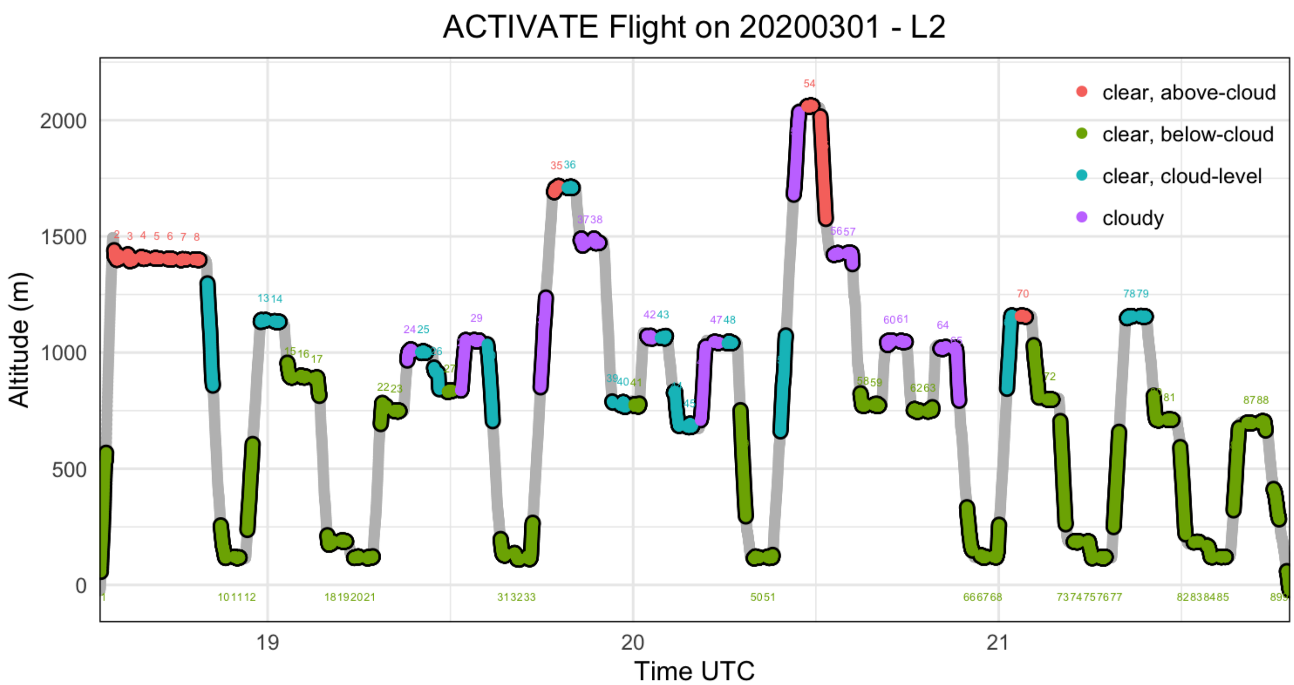

Figure S1. Categorization of CCN measurements during RF14 on 1 March 2020 as defined in Section 2.1.

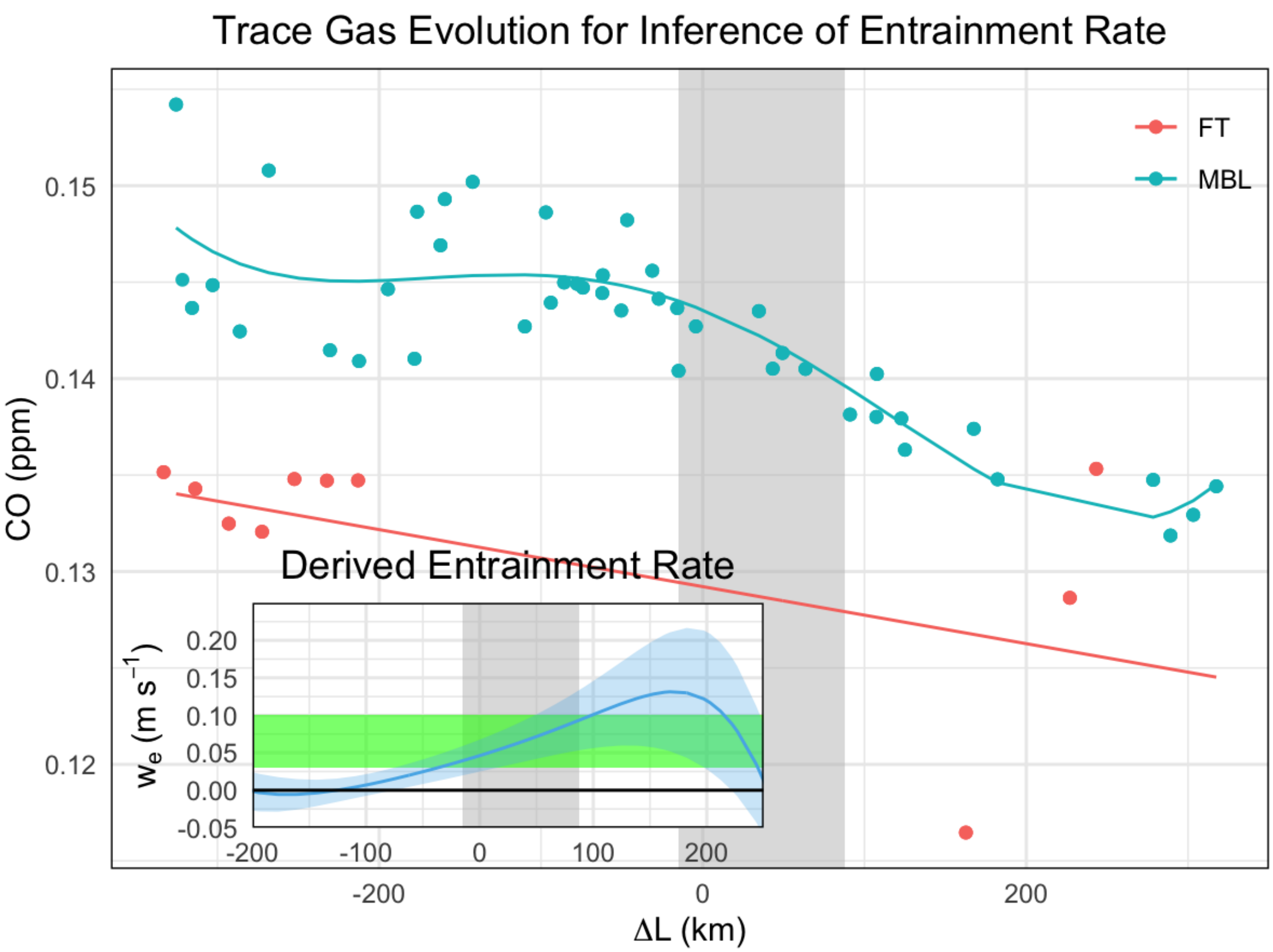

Figure S2. CO trace gas measurements during RF14 on 1 March 2020 as a function of distance from cloud edge (ΔL) sorted into altitudes relative to the cloud deck (see legend). Inset: entrainment rates derived from mixed-layer framework (blue) with shaded uncertainties (plus/minus one sigma), and the range found in large-eddy simulations of a similar case (green shading; Tornow et al., 2021). Gray shading indicates distance range of budget analysis.

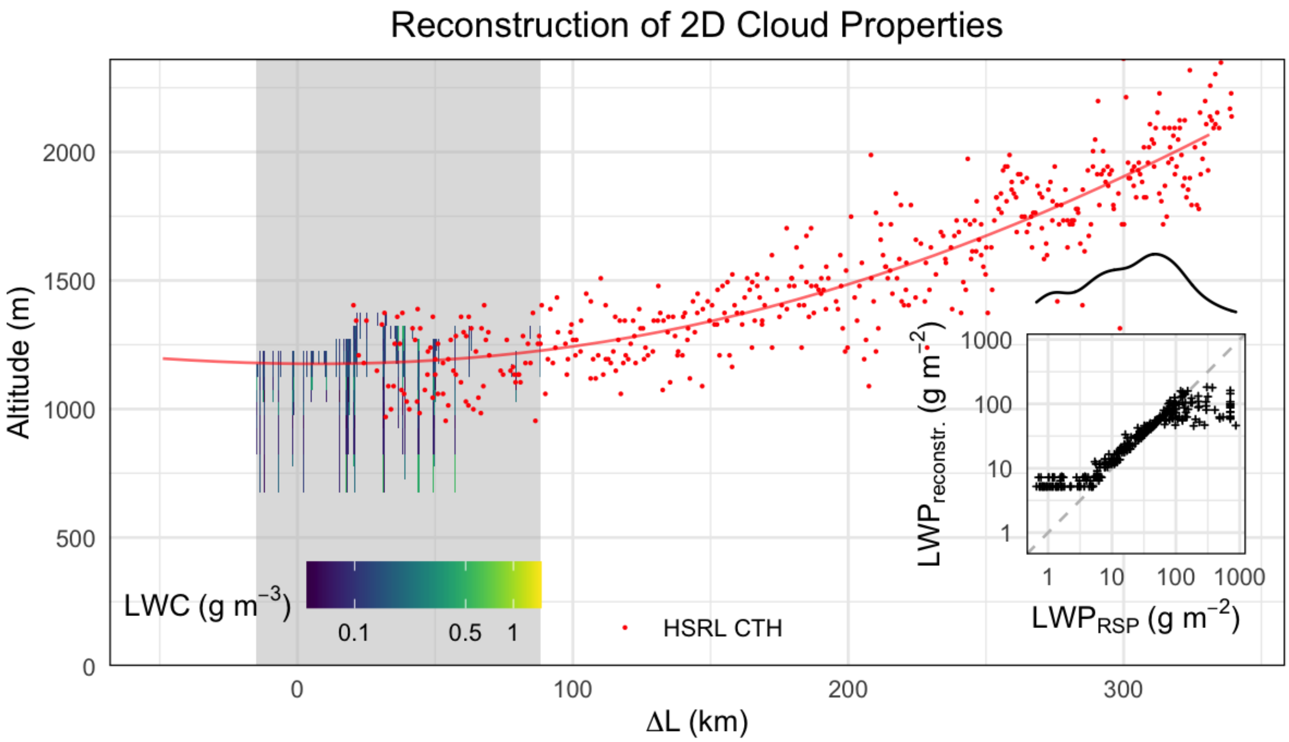

Figure S3. Overview of RF14 (1 March 2020) mock-cloud-profiles (LWC shown as colored shading) together with HSRL-2 cloud-top heights (red). The inset compares LWP from reconstructed profiles with the RSP-based LWP values. The curve above the inset indicates the probability density function for RSP-based values.

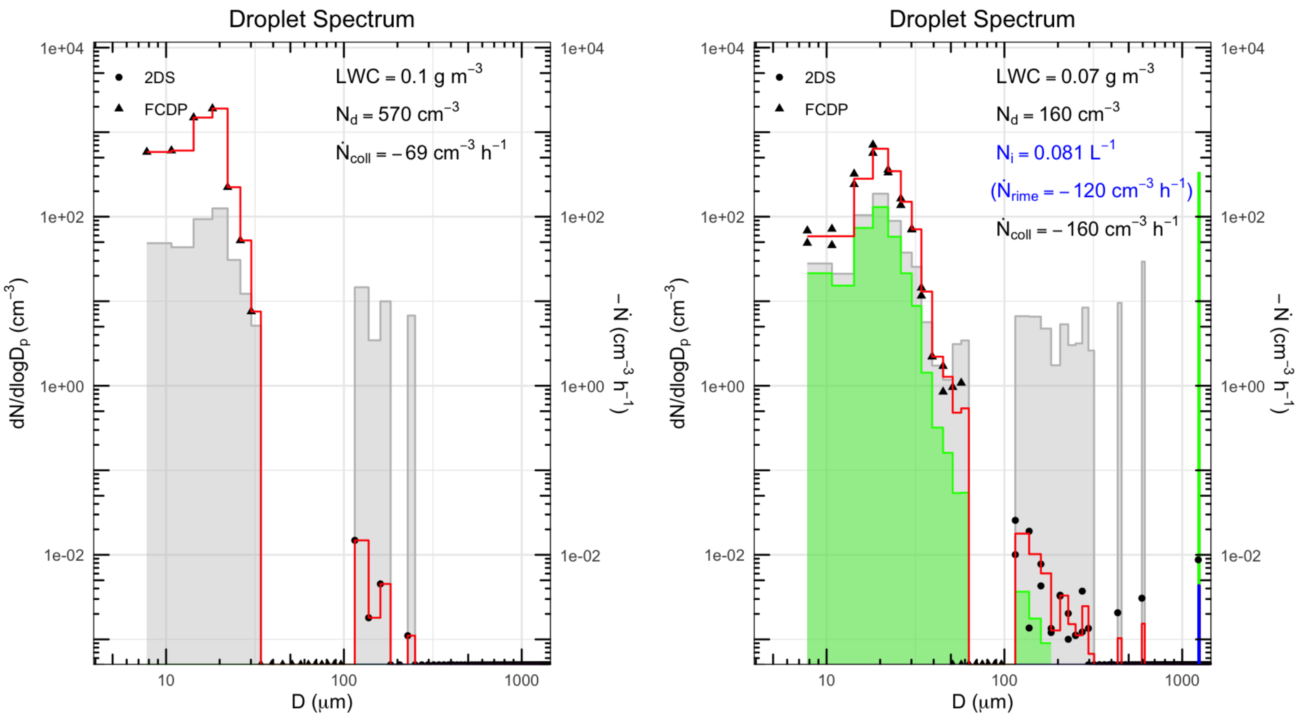

Figure S4. Example hydrometeor size distributions (red, scale on left axes) during RF14 at flight time 70495 s (left) and at 73525 s (right) and corresponding computed collision loss rates (listed at top-right corner) with bin-wise contributions (gray shade, scale on right axes). Rates that involved hydrometeors classified as frozen (only in one bin, shown with blue bar) are labelled as "riming" (shown as integral in blue text and as bin-wise contribution through green shading).

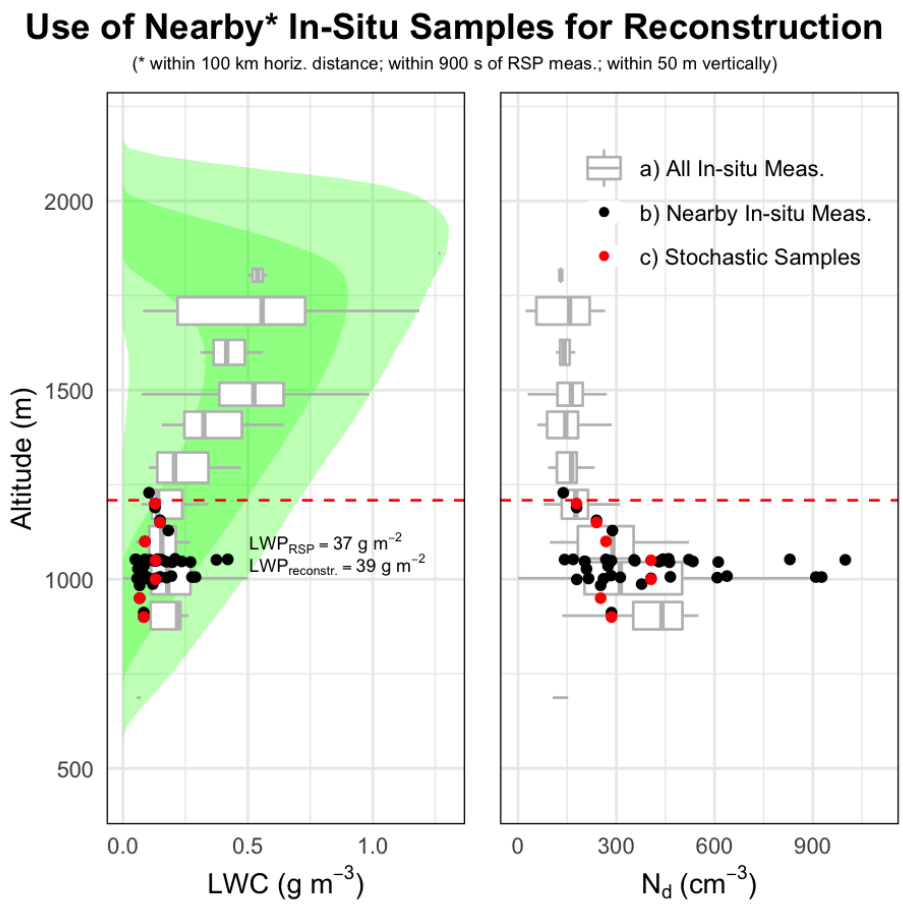

Figure S5. Example of RF14 (1 March 2020) in-situ samples (black) to stochastically build a mock-cloud-profile (red), shown for LWC (left) and N_d (right), until the LWP roughly matches the nearby RSP-sampled value. Gray bars mark the range of all in-situ observations (box ranging between 25$^{\text{th}}$ and 75$^{\text{th}}$ percentiles and whiskers extending to 5$^{\text{th}}$ and 95$^{\text{th}}$ percentiles). The green shading (lighter shade marks 5$^{\text{th}}$ to 95$^{\text{th}}$ and darker shade 25$^{\text{th}}$ to 75$^{\text{th}}$ percentiles) shows LWC profiles from large-eddy simulations of a similar case (altitudes shifted 500 m downward). The decrease of N_d with height is an artifact of MBL deepening downwind where N_d progressively decreases.

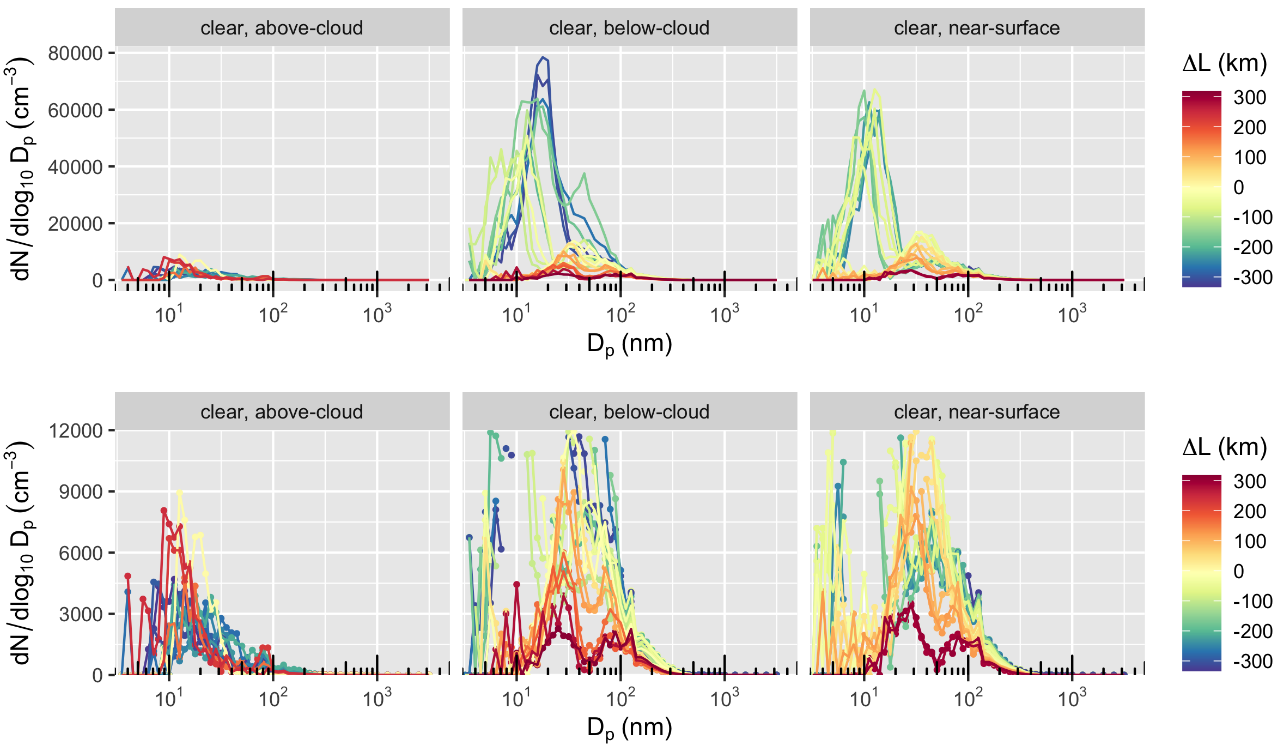

Figure S6. Aerosol particle size distributions measured during RF14 (1 March 2020) in the FT and MBL (top; and with reduced y-axis range, bottom). Colors mark the downwind distance from cloud edge, ΔL.

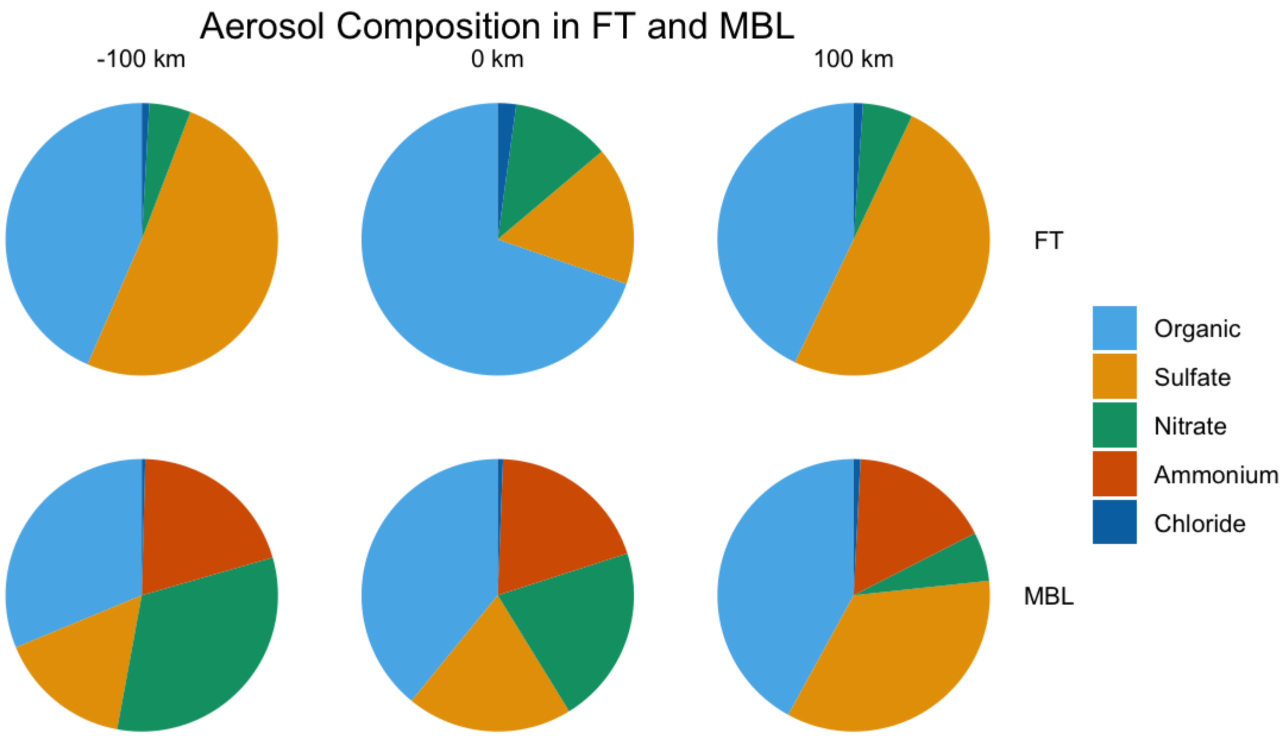

Figure S7. Aerodyne High-Resolution Mass Spectrometer (AMS) measurements during RF14 (1 March 2020) for the approximate size range 60-600 nm, showing mass proportions in FT (top) and MBL (bottom) air masses and were interpolated to three selected ΔL values (horizontal position).

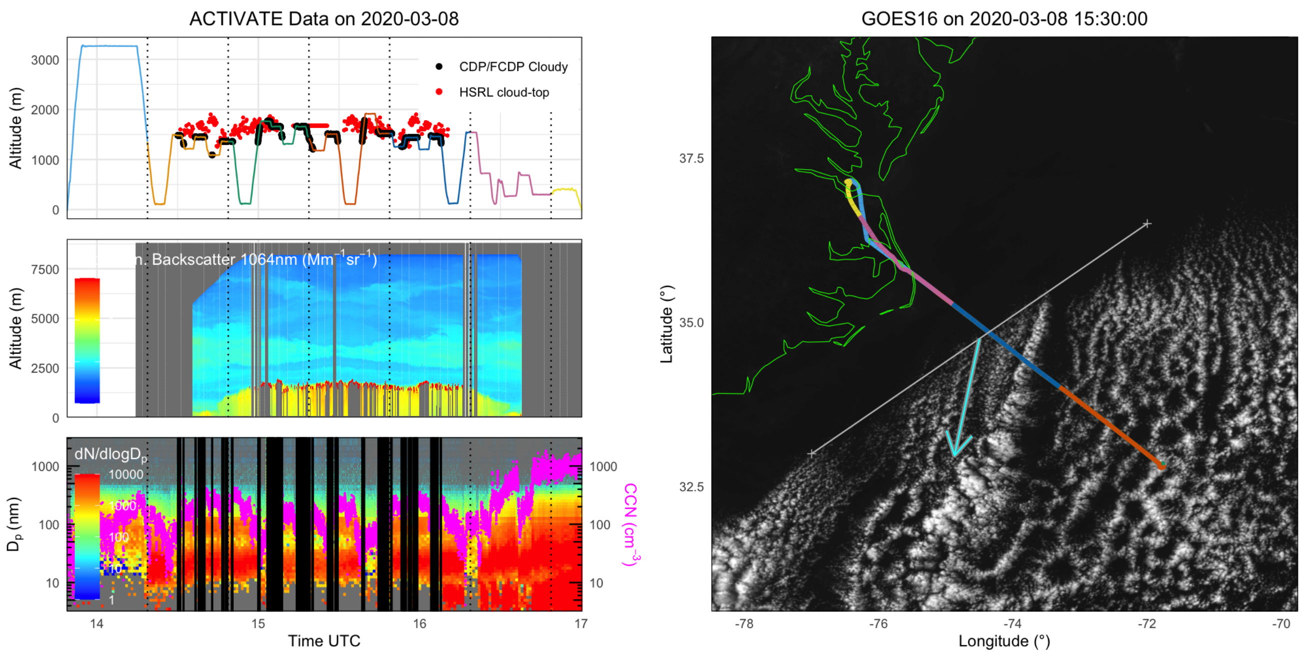

Figure S8. As in Figure 1, but for the first research flight on 8 March 2020 (RF17).

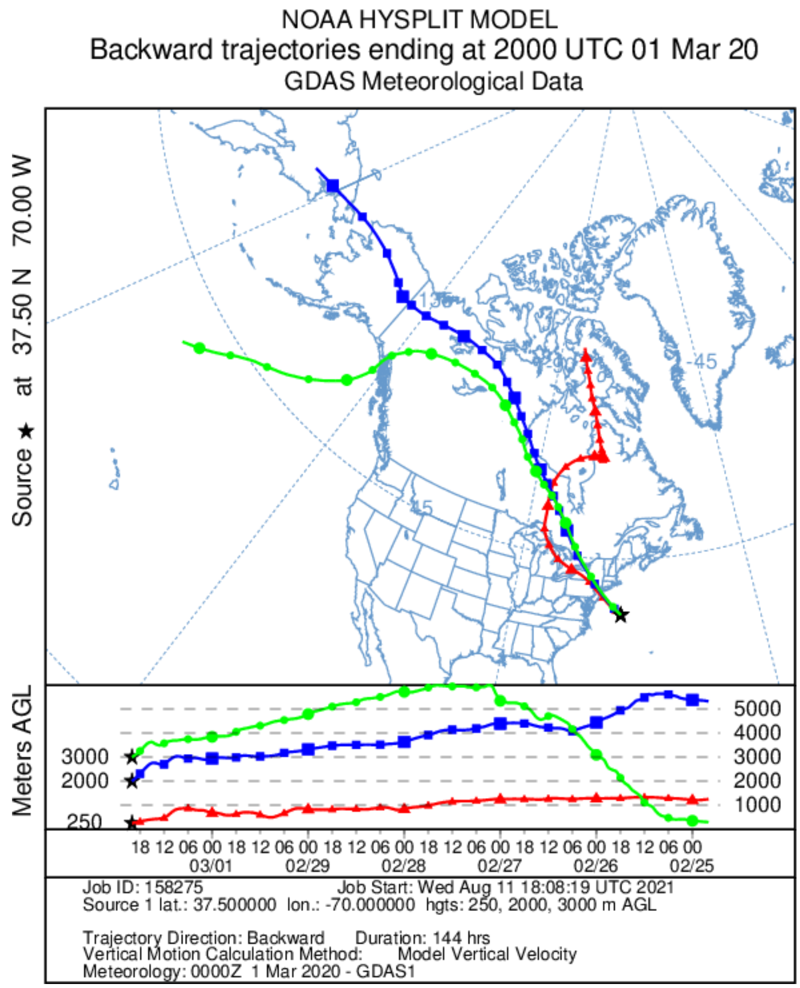

Figure S9. Back-trajectories based on HYSPLIT (Stein et al., 2015; Rolph et al., 2017) for RF14.